

Thiocyanate-Modified Silver Nanofoam for Efficient CO₂ Reduction to CO

Li Wei,* Hao Li, Junsheng Chen, Ziwen Yuan, Qianwei Huang, Xiaozhou Liao, Graeme Henkelman, and Yuan Chen*



Cite This: *ACS Catal.* 2020, 10, 1444–1453



Read Online

ACCESS |



Metrics & More



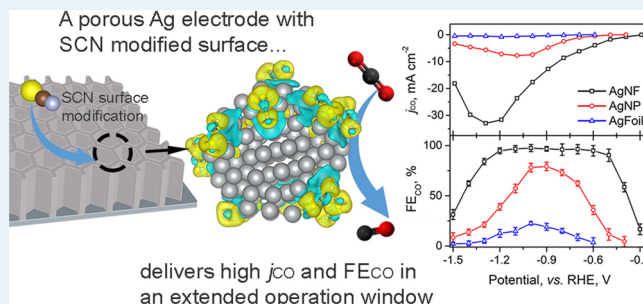
Article Recommendations



Supporting Information

ABSTRACT: Ag is a promising electrocatalyst for electrochemical reduction of CO₂ to CO due to its relatively low cost and high activity. However, it is challenging to achieve high reaction rates while maintaining good selectivity. Here, we used an H₂ bubble-templated electrodeposition method in a thiocyanate (SCN)-containing aqueous electrolyte to synthesize a hierarchically porous Ag nanofoam (AgNF) with curved Ag surfaces modified by SCN. This AgNF demonstrates excellent performance for CO₂ reduction with a high CO Faradaic efficiency (FE_{CO}) of 97%. It can maintain over 90% FE_{CO} in a wide potential window (−0.5 to −1.2 V_{RHE}), enabling the maximum CO selective current density of 33 mA cm^{−2} and the mass activity of 23.5 A g_{Ag}^{−1}, which are the highest values among recently reported Ag-based electrocatalysts. Mechanism studies reveal that the catalytic performance of the AgNF correlates with the density of surface SCN ligands, which exhibit excellent electrochemical stability under negative potentials. Density functional theory calculations suggest that SCN ligands promote the formation of COOH* intermediates by modifying the local electron density at the active sites. Further, the synthesis method is applicable to different catalyst substrates. For example, the AgNF grown on a carbon-based gas diffusion film exhibits an ultrahigh mass activity of 52.1 A g_{Ag}^{−1} and maintains its high CO selectivity simultaneously, demonstrating excellent potentials for practical applications.

KEYWORDS: silver, nanofoam, thiocyanate, CO₂ reduction, electrodeposition



INTRODUCTION

The fast increasing atmospheric carbon dioxide (CO₂) concentration is a critical challenge for human society.^{1,2} A sustainable solution is to electrochemically reduce CO₂ to useful chemical species, such as carbon monoxide (CO), formic acid, methanol, ethylene, or methane, using electrical energy generated from renewable sources.^{3–10} In particular, CO can be used as fuels or feedstocks for producing chemicals via the Fischer–Tropsch process.^{11,12} The electrochemical reduction of CO₂ to CO follows a two-electron reduction pathway: CO₂ + 2H⁺ + 2e[−] = CO + H₂O with a relatively low redox potential of −0.53 V versus the standard hydrogen electrode (SHE). Hydrogen evolution reaction (HER) in aqueous electrolytes is a critical competitive reaction of CO₂ reduction reaction (CO₂RR), which significantly compromises the selectivity to CO and reduces the efficiency of CO₂RR devices.¹³ An ideal electrocatalyst for CO₂RR is expected to deliver a large current density and maintain a high selectivity toward desired reduction products.

Silver (Ag) is a promising electrocatalyst for CO₂RR to CO due to its relatively low cost and high activity. A simple Ag foil can achieve a Faradaic efficiency toward CO (FE_{CO}) of more than 60%.¹⁴ Recent studies show that the performance of Ag-

based electrocatalysts can be significantly improved by tailoring their physical structures and surface chemical compositions.^{14–21} For physical structures, the catalytic activity of Ag nanoparticles (AgNPs) displays a volcano-shaped trend for CO₂RR over the size of the AgNPs.¹⁹ Triangular Ag nanoplates with Ag(100) facets show superior selectivity and activity as compared to AgNPs.²² Highly curved Ag nano-channels created by an alloying–dealloying method have a high FE_{CO} of 90% at −0.8 V_{RHE}.^{16,23} At the optimal thickness of ~6 μm, nanoporous Ag thin films can deliver a maximum Ag mass activity of 12.2 A g_{Ag}^{−1}.²⁴ For surface chemical composition modifications, Ag surfaces modified by Cl[−], S^{2−}, or phosphate anions^{17,21,25} or small molecules, such as cysteamine,²⁶ ethylenediamine, oleylamine, or 1-dodecanethiol,²⁷ have demonstrated improved selectivity to CO than unmodified Ag surfaces. The stability of surface modification agents on Ag surfaces under cathodic potentials is essential in

Received: October 27, 2019

Revised: December 19, 2019

Published: December 20, 2019

maintaining the high CO selectivity.²⁸ Current surface modification agents can only retain the high CO selectivity (>90%) at relatively low potentials, that is, $-0.9 V_{\text{RHE}}$, affording the highest mass activity of $2.56 A g_{\text{Ag}}^{-1}$ from cysteamine-modified AgNPs.²⁶ We noticed that thiocyanate (SCN) exhibits strong interactions with Ag, and it is electrochemically stable even under negative potentials.²⁹ Further, as a pseudohalide, SCN may introduce covalency to electrocatalysts, which could be beneficial for the adsorption of intermediates in CO_2RR .^{28–31} However, SCN has not been used to modify Ag electrocatalysts for CO_2RR .

Herein, we first used a dynamic hydrogen bubble-templated electrodeposition method to create a free-standing three-dimensional porous Ag nanofoam (denoted as AgNF),^{32,33} which is engraved with abundant curved surfaces and surface SCN ligands. The catalytic performance of this AgNF for electrochemical reduction of CO_2 was evaluated together with several reference Ag electrocatalysts, including Ag nanoparticles (AgNPs), Ag foils, and AgNFs with different densities of surface SCN ligands. The roles of SCN ligands were investigated by Raman spectroscopy. Further, density functional theory (DFT) calculations were carried out to gain a better understanding of the catalytic function of AgNF.

EXPERIMENTAL SECTION

Electrodeposition of SCN-Modified AgNF. Ag foil (99.99%, 0.1 mm thick, Sigma-Aldrich) was first cleaned by washing with diluted HNO_3 . Next, SCN-modified AgNF was electrodeposited on the cleaned Ag foil in a three-electrode configuration on an electrochemical workstation (CHI 660E). A Pt gauze and a Ag/AgCl electrode (3 M KCl) acted as the counter and reference electrodes, respectively. The plating area is $0.5 \times 0.5 \text{ cm}^2$ on one side of the Ag foil while an insulating adhesive sealed the other side. A mixture of Ag_2SO_4 (99.99%, Sigma, 0.01 M), KSCN (99%, Sigma, 1.5 M), and $(\text{NH}_4)_2\text{SO}_4$ (99.9%, Sigma, 0.5 M) aqueous solutions served as the electrolyte. The deposition current density was $-1 A \text{ cm}^{-2}$, and the deposition time was 20 s. It should be noted that a two-chamber cell was used for electrodeposition of AgNF. The cells are physically separated by glass frits (5 mm) to avoid possible Pt contamination. Pt is absent from AgNF as confirmed by X-ray photoelectron spectroscopy (XPS) spectra in the Pt 4f region. After the electrodeposition, the AgNF was further cycled in the electrolyte between -0.5 and $0.2 V$ versus Ag/AgCl at a scan rate of 50 mV s^{-1} for 30 cycles before it was rinsed with deionized (DI) water and dried in a vacuum overnight. A silver mass loading of $\sim 1.45 \text{ mg cm}^{-2}$ was determined by weighing the electrode before and after deposition. The electrodeposition of AgNF on the gas diffusion electrode was performed under the same condition.

Synthesis of AgNPs. AgNPs were synthesized using a previously reported method.¹⁷ In brief, the AgNO_3 solution (100 mL of 10 mg mL^{-1}) was mixed with citrate trisodium solution (100 mL of 5 mg L^{-1}) under stirring. After 30 min, NaBH_4 solution (50 mL of 20 mg mL^{-1}) was added. The resulting solid materials were recovered after 2 h, washed with DI water, and then tip sonicated in 250 mL of DI water for 2 h before the Ag NP suspension was further centrifuged at 4000 g for 1 h. The resulting supernatant was drop cast on a carbon cloth to reach a mass loading of 1.45 mg cm^{-2} , matching the mass loading of AgNF on the Ag foil electrodes.

Material Structural Characterization. Physical structures of synthesized materials were examined by a scanning

electron microscope (SEM, Joel JSM-6700F) and a transmission electron microscope (TEM, FEI Themis-Z). Their Raman spectra were collected on a Raman microscope (Renishaw inVia) using a 785 nm laser. X-ray diffraction (XRD) patterns of AgNF deposits scratched off from substrates were recorded on an XRD diffractometer (Bruker AXS D8). XPS spectra were obtained on a Thermo Scientific K-Alpha spectrometer with a Al $K\alpha$ (1486.3 eV) source.

Fabrication of AgNF with Reduced SCN Surface Density. The electrochemical reduction of AgNF was carried out in an Ar-saturated KHCO_3 electrolyte (0.5 M) using the same three-electrode configuration used for electrodeposition. The reduction was performed under two different potentials for 30 min before the AgNF electrode was rinsed with DI water and dried in ambient condition. The electrodes reduced at -1.0 and $-1.4 V_{\text{RHE}}$ were denoted as AgNF-R1 and AgNF-R2, respectively.

Electrochemical reduction of CO_2 and Product Analysis. All CO_2 electrochemical reduction tests were carried out on the electrochemical workstation (CHI 660E) using a gas-tight H-shaped two-compartment cell separated by a preactivated membrane (Sigma-Aldrich, Nafion 117). Each compartment contains 60 mL of 0.5 M KHCO_3 as the electrolyte, and the headspace is about 30 mL. The electrolyte was stirred at 400 rpm using a PTFE-covered magnetic bar. The electrolyte was first saturated with Ar and pre-electrolyzed with a Pt electrode at $-0.3 V_{\text{RHE}}$ for 30 min before saturation with CO_2 for the tests. A Pt gauze and a Ag/AgCl (3 M KCl) electrode served as the counter and reference electrodes, respectively, in one compartment, while a AgNF electrode was used as the working electrode in the other compartment. Chronoamperometric current–time ($i-t$) curves were recorded at different potentials. All potentials were calibrated to RHE by adding $0.210 + 0.0591 \times \text{pH}$. The pH value of the electrolyte after saturation with CO_2 was measured by a pH meter (Horiba, PC1100). Tafel plots were compiled from stable CO specific current densities at various potentials after 2 h testing. The gaseous products were analyzed on a gas chromatograph (Agilent 6890 N) using PLOT MolSieve 5A and Q-bond PLOT capillary column with He (99.999%) as the carrier gas.

Determination of Electrochemical Active Surface Area (ECSA). The ECSA of Ag electrodes was determined by comparing electrons required to form a monolayer of Ag_2O or $\text{Ag}(\text{OH})$ on the Ag surface in a three-electrode configuration using Ar-saturated 0.1 M KOH as the electrolyte.¹⁸ A Ag/AgCl (3 M KCl) electrode and a Pt gauze were used as the reference and counter electrodes, respectively. The working Ag electrodes were first electrochemically reduced at $-0.8 V_{\text{RHE}}$ for 10 min and rinsed with DI water. Afterward, they were oxidized at $1.15 V_{\text{RHE}}$ in a fresh 0.1 M KOH electrolyte for 10 min, during which a monolayer of Ag was oxidized to form Ag_2O or $\text{Ag}(\text{OH})$. The charge required to form such a monolayer is about $400 \mu\text{C cm}^{-2}$. The current–time ($i-t$) curves for the oxidation of AgNF, AgNP, and Ag foil electrodes were recorded.

Density Functional Theory (DFT) Calculations. All DFT calculations were conducted using the Vienna ab initio simulation package (VASP). The electronic exchange was described by a generalized gradient approximation method. The electronic correlation was described with a Perdew–Burke–Ernzerhof functional.³⁴ Core electrons were described by a projector augmented-wave method.³⁵ The valance

electrons were described by expanding the Kohn–Sham wave functions in a plane wave basis.³⁵ Gamma point sampling of the Brillouin zone was used for the calculations of Ag clusters. The Brillouin zone for the model of Ag(111) was sampled using a $(3 \times 3 \times 1)$ Monkhorst-Pack k -point mesh and integrated using the method by Methfessel and Paxton.³⁶ The energy cutoff for the calculations was set at 400 eV, and the force convergence criteria were set as 0.05 eV Å⁻¹. Spin polarization was tested and was found to have a negligible influence on the results. Zero-point energy and entropic corrections (with a temperature of 298 K) were applied to the calculated reaction energies. The integrated heat capacity corrections were applied using the values obtained by Gao and co-workers.³⁷ The initial geometry of the Ag clusters was assumed to have a 147-atom cuboctahedral shape. Thiocyanates were modeled at the truncated corner sites, similar to a previous study.²⁶ The Ag(111) surface was modeled as a three-layer (5×5) slab with the bottom layer fixed in bulk position.

RESULTS AND DISCUSSION

A dynamic H₂ bubble-templated electrodeposition method was used to synthesize AgNF with a hierarchical porous structure.³⁸ The electrodeposition was carried out under a current density of -1 A cm^{-2} for 20 s on one side of prepolished Ag foils. The electrodeposition of Ag was accompanied by vigorous H₂ bubble formation, coalescence, and dissipation, resulting in AgNF with interconnected mesopores and macropores, which avoids the use of solid templates and their removals. $(\text{NH}_4)_2\text{SO}_4$ was used as the electrolyte for electrodeposition to prevent the possible incorporation of halide ions (e.g., Cl⁻).^{32,33} After the electrodeposition, the shining Ag foils were coated by a layer of AgNF in grey color with a mass loading of 1.45 mg cm⁻². AgNPs with a diameter of $\sim 10 \text{ nm}$ were also prepared as a reference. Figure S1 in the Supporting Information shows their SEM and TEM images.

The morphology of AgNF was first examined by SEM. Figure 1a reveals abundant macropores with a diameter of about 20 μm , which were created by the dissipation of large H₂

bubbles. These macropores not only expose the inner space of the AgNF but also can facilitate mass transportation of molecules/ions in electrolytes and gas bubbles during CO₂RR. The higher magnification SEM image in Figure 1b displays interconnected Ag ligaments, which form mesopores of less than 50 nm in diameter. These pores with highly curved surfaces are similar to those reported previously using an alloying–dealloying method, which demonstrated high selectivity in reducing CO₂ to CO.¹⁶ We further characterized the structure of the AgNF by TEM. The inset of Figure 1c displays the selected area diffraction pattern of Ag ligaments with various diffraction rings, which can be assigned to multiple Ag facets. Figure 1d displays TEM images collected at a higher magnification. The Ag lattice fringes with a d -spacing of 0.23 nm are from Ag(111). The corresponding Fourier-transformed image shows a highly symmetric pattern, suggesting an extended crystalline network. A thin layer ($\sim 1 \text{ nm}$) with poor crystallinity was found at the Ag ligament surface, which exhibited reduced contrast under the high-angle annular dark-field mode scanning TEM (HAADF-STEM, Figure 1e) as a result of surface modification. The corresponding elemental mappings obtained by the energy-dispersive X-ray spectroscopy (EDX) confirm the existence of S, C, N, and O on the surface Ag ligaments. S and N distribute uniformly on the Ag surface. The overlaid Ag and S signals indicate that S is enriched at the surface. Overall, the TEM characterization results indicate the existence of surface-anchored S, C, and N species.

The XRD pattern of AgNF was obtained by measuring Ag deposits scratched from Ag foils to avoid strong XRD signals from the substrates. Figure 2a shows four predominant diffraction peaks ($2\theta = 38.2^\circ, 44.4^\circ, 64.5^\circ, \text{ and } 77.4^\circ$), which originate from various Ag crystal facets (PDF#04-0783), agreeing with the SAED pattern shown in Figure 1c. The inset of Figure 2a shows the magnified XRD pattern at the low diffraction angle region ($2\theta = 10^\circ$ to 40°). The weak peak of Ag₂O ($2\theta = 32.8^\circ$, PDF#41-1104) suggests some surface oxidation by O₂ dissolved in electrolytes or oxidation in air. No XRD features belonging to bulk AgSCN (PDF#36-0608) or AgCl (PDF#22-1326) are observed. Raman and X-ray photoelectron spectroscopies were used to elucidate the chemical configurations of S, C, and N. Figure 2b displays the Raman spectrum of AgNF, showing three features at δ_{SCN} (443 cm^{-1}), ν_{CS} (723 cm^{-1}), and ν_{CN} (2112 cm^{-1}) originated from thiocyanate.³⁹ Some weak Raman features at $1000\text{--}1500 \text{ cm}^{-1}$ can be attributed to surface Ag₂O. Meanwhile, there are no Raman features from Ag–S compounds, such as Ag₂S, Ag₂SO₃, or Ag₂SO₄.^{40,41} The XPS survey scan spectrum in Figure 2c indicates the existence of S, C, and N on the AgNF surface with the abundance of 2.19, 1.96, and 2.28 at %, respectively, which indicate an average coverage of 0.1884 SCN per surface Ag atom (see Figure S2 and the related calculation in the Supporting Information). The high-resolution XPS spectra of S, C, and N in Figure 2d are similar to those of the reference AgSCN (Figure S3 in the Supporting Information). Besides, no features from S–O are observed in the high binding energy region ($\sim 168 \text{ eV}$), indicating that S atoms exist in SCN ligands on the AgNF. Moreover, the featureless XPS spectrum collected in the Cl 2p region rules out the presence of Cl in the AgNF (Figure S4 in the Supporting Information).

The performance results of AgNF, AgNPs (1.45 mg cm⁻²), and Ag foil for CO₂RR were compared in a 0.5 M KHCO₃

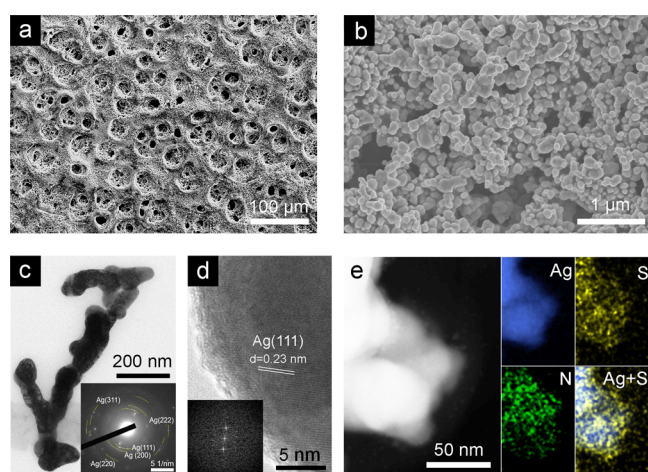


Figure 1. Morphology and chemical composition of AgNF. (a, b) SEM images of AgNF at different magnifications. (c, d) Bright-field TEM images at different magnifications. The inset of (c) shows the corresponding diffraction pattern, and the inset of (d) is the Fourier-transformed image. (e) HAADF-STEM image and its corresponding EDX elemental mapping results. Ag and S signals are overlaid for comparison.

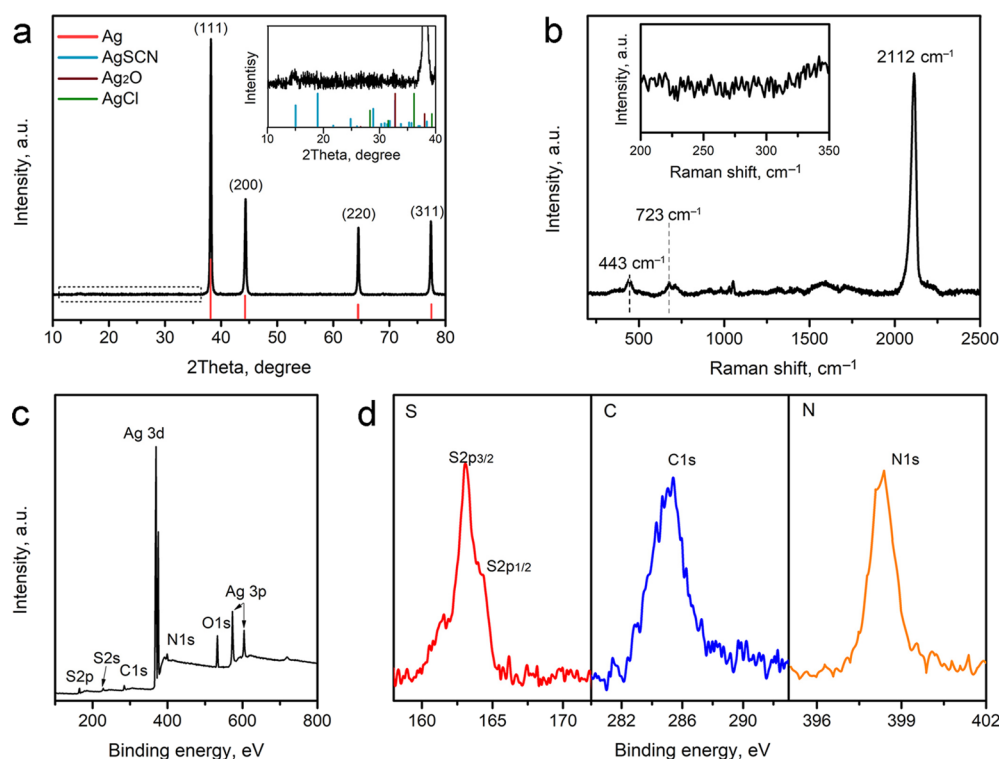


Figure 2. (a) XRD pattern and (b) Raman spectrum of AgNF. (c) XPS spectrum of a survey scan and (d) the high-resolution XPS spectra of C, N, and S.

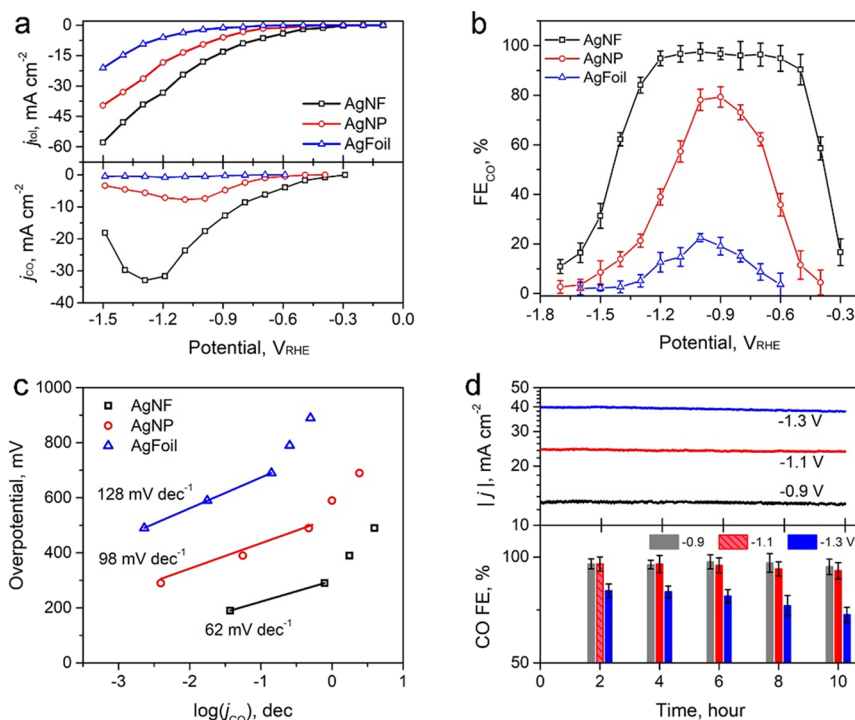


Figure 3. Performance of three types of Ag electrodes, i.e., AgNF, AgNP, and Ag foil, for electrochemical CO₂RR. (a) Total current density (j_{tot} , top) and j_{CO} (bottom), and (b) FE_{CO} obtained at different potentials. (c) Tafel plots constructed from the measured CO partial current densities. (d) Stability tests of AgNF performed at -0.9 , -1.1 , and -1.3 V_{RHE} .

electrolyte by measuring their chronopotentiometric discharges under different potentials (-0.3 to -1.5 V_{RHE}) over a 2 h period. Gaseous products were analyzed by gas chromatography every 30 min. CO and H₂ were identified as the main reaction products. Small amounts of CH₄, C₂H₄, and

formate were also detected when the applied potential is more negative than -1.4 V_{RHE} . Figure 3a shows the quasi-polarization curves, which were constructed using steady-state currents extracted from i - t curves collected under different applied potentials. The AgNF outperforms both

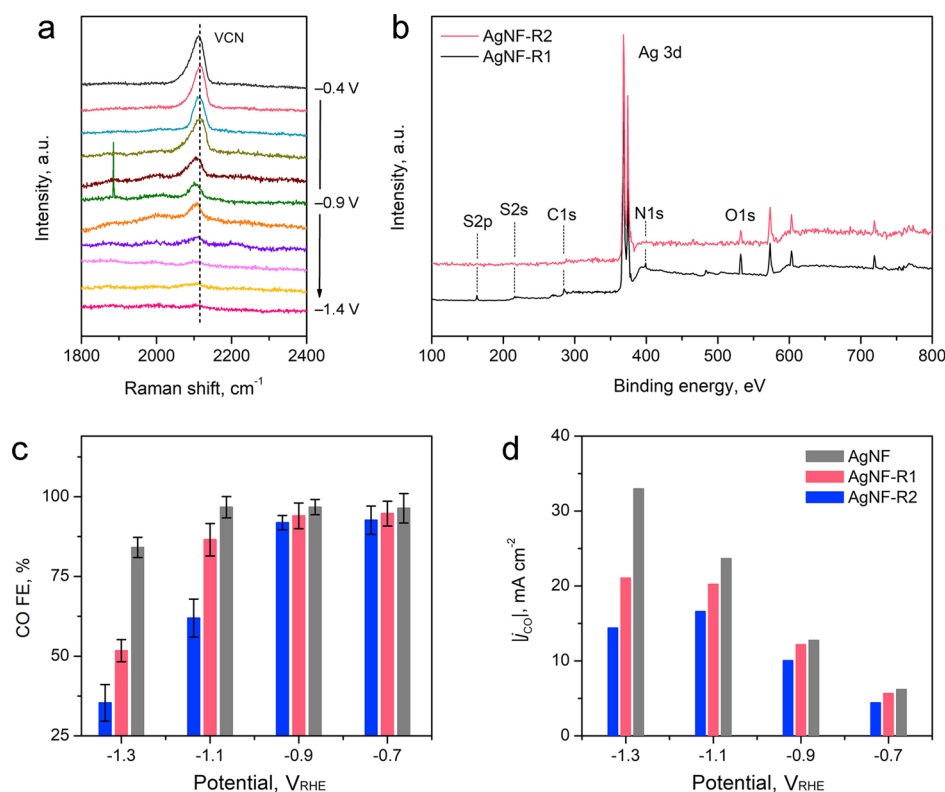
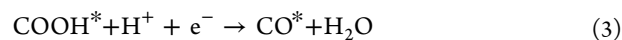


Figure 4. Characterization and performance of CO₂ electrochemical reduction of AgNF-R1 and AgNF-R2. (a) Raman spectra of AgNF collected after CO₂ electrochemical reduction under different potentials. (b) XPS survey scan spectra of AgNF-R1 and AgNF-R2. (c) FE_{CO} and (d) *j*_{CO} of AgNF, AgNF-R1, and AgNF-R2 under different potentials.

AgNP and Ag foil in the potential window from -0.2 to -1.5 V_{RHE}, demonstrating much higher total density (*j*_{tot}) and CO specific current density (*j*_{CO}). Typical current–time (*i*–*t*) curves collected at -1.2 V were shown in Figure S5 in the Supporting Information together with their calculated FE_{CO}. We also compared the FE_{CO} and FE_{H₂} of AgNF, AgNPs, and Ag foil in Figure S6 in the Supporting Information. The AgNF delivered a high *j*_{tot} of -33.4 mA cm⁻² together with a high FE_{CO} of $94.8 \pm 2.9\%$. Both values are much higher than those of AgNPs (-18.4 mA cm⁻² and $39.0 \pm 3.3\%$) and Ag foil (-6.1 mA cm⁻² and $12.6 \pm 3.9\%$). FE_{CO} at different potentials is plotted in Figure 3b. CO can be detected in gaseous products at merely -0.3 V_{RHE} on the AgNF, which is 0.1 and 0.3 V less than those of AgNP and Ag foil, respectively. The FE_{CO} of AgNF increased quickly to 90% at -0.5 V_{RHE} and maintained around 95% when the potential went down to -1.2 V_{RHE}. In comparison, both AgNPs and Ag foil displayed not only lower maximum FE_{CO} but also narrower potential windows in which they can maintain the high CO selectivity. The AgNF exhibits the highest *j*_{CO} of -33.0 mA cm⁻² at -1.3 V_{RHE} and it can work in a significantly extended the operation window and deliver the high current density while maintaining high selectivity to CO. Further, the corresponding mass activity of 23.5 A g_{Ag}⁻¹ toward CO is one of the highest among recently reported Ag-based electrocatalysts for CO₂RR.^{16,17,20} We further compared *j*_{CO-ECSA} of Ag electrodes by normalizing their CO specific current density obtained at -0.6 V_{RHE} to their surface roughness factor (Figure S7 in Supporting Information).¹⁶ The *j*_{CO-ECSA} of AgNF is -33.6 μA cm⁻², which is 9 and 60 times higher than those of AgNPs (-3.7 μA cm⁻²) and Ag foil (-0.54 μA cm⁻²), respectively. This result indicates that AgNF has significantly improved intrinsic

catalytic activity (see Table S2 in the Supporting Information for comparison with recently reported Ag-based electrocatalysts).

The CO₂ reduction kinetics on the Ag electrodes was analyzed using their Tafel plots. Figure 3c shows that AgNF has a Tafel slope of 62 mV dec⁻¹, which is much lower than those of AgNPs at 92 mV dec⁻¹ and Ag foil at 128 mV dec⁻¹, indicating better reduction kinetics. The commonly proposed reaction mechanism of electrochemical reduction from CO₂ to CO involves the formation of reaction intermediates, such as CO₂*⁻ and COOH*, following the four steps shown below



The Tafel slope of 62 mV dec⁻¹ from AgNF suggests the rate-limiting step is the proton-coupled step (eq 3). While the larger Tafel slopes of AgNPs and Ag foil indicate that the rate-limiting step is the initial surface adsorption of CO₂ (eq 1).^{17,23} The catalytic stability of AgNF was also evaluated by measuring their chronopotentiometric discharges under -0.9 , -1.1 , and -1.3 V_{RHE} over 10 h. Figure 3d shows that the current density decreases merely 2.3, 4.5, and 9.6%, respectively. Further, FE_{CO} remains mostly unchanged throughout the tests under -0.9 and -1.1 V_{RHE}. However, after the 8 h test under -1.3 V_{RHE}, FE_{CO} drops to 77.1%. SEM images of AgNF after the stability tests are shown in Figure S8 in the Supporting Information. There are minor structural

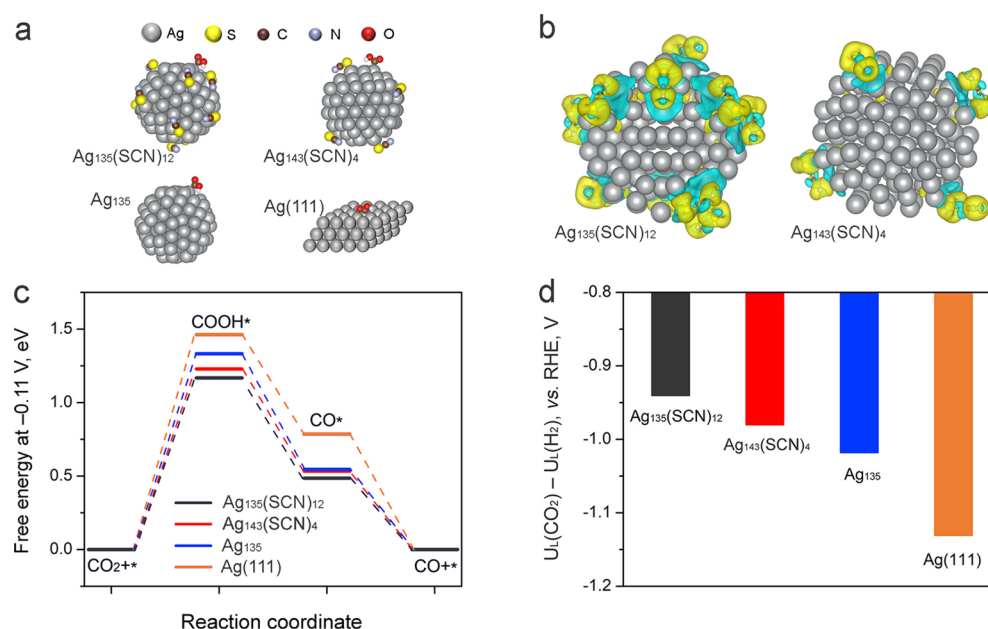


Figure 5. Reaction mechanism investigated by DFT calculations. (a) Ag catalyst models used in the DFT calculations. (b) Charge density redistribution on the Ag surfaces anchored by SCN ligands. (c) Free energy pathways of CO₂ reduction at the equilibrium potential (-0.11 V) on Ag₁₃₅(SCN)₁₂, Ag₁₄₃(SCN)₄, Ag₁₄₇, and Ag(111) surfaces. (d) The difference in limiting potentials (ΔU_L) of CO₂ reduction and HER on the Ag catalyst surfaces.

changes, except for the slight aggregation of Ag ligaments after the test under -1.3 V_{RHE}.

We further studied the potential roles of SCN ligands in improving the intrinsic catalytic activity of AgNF. The stability of SCN ligands anchored on the Ag surface at different potentials was first evaluated by Raman spectroscopy. As shown in Figure 4a, the intensity of the Raman peak of SCN ligands (i.e., the ν_{CN} peak at 2112 cm⁻¹) has a minor decrement when the applied potential drops to -1 V_{RHE}, indicating the excellent stability of SCN ligands. Further decreasing the potential leads to the fast intensity drop of the ν_{CN} peak.

The Raman peak diminishes under -1.4 V_{RHE}, which coincides with the quickly deteriorated FE_{CO} shown in Figure 3b. To examine the relationship between SCN ligands anchored on the Ag surface and the catalytic activity of AgNF for CO₂ reduction, two additional AgNF electrodes with reduced SCN ligand densities were prepared by cathodically reducing AgNF electrodes at -1.0 and -1.4 V_{RHE} in Ar-saturated 0.5 M KHCO₃ electrolytes, denoted as AgNF-R1 and AgNF-R2, respectively. The XPS survey scan spectra of AgNF-R1 and AgNF-R2 in Figure 4b confirm their surface composition changes. The S concentration on AgNF-R1 drops to 0.41 at %, which is about 19% of the S concentration on AgNF before the cathodic reduction. The C and N concentrations on AgNF-R1 also decreased. In comparison, the XPS signals of S, C, and N are undetectable on AgNF-R2, suggesting that all SCN ligands were removed. The high-resolution Ag 3d XPS spectra of AgNF electrodes in Figure S9 in the Supporting Information show the formation of a Ag⁰ surface after the removal of SCN ligands and the reduction of surface oxide layers upon the reduction treatment. Figure S10 shows that high-resolution XPS spectra of S, C, and N of AgNF-R1 are similar to that of AgNF, indicating that they still exist in the thiocyanate configuration. HAADF-STEM images in Figure S11 show that the morphologies of Ag ligaments in

AgNF and AgNF-R1 are similar. The EDX mapping results also agree with the XPS results, displaying reduced S concentrations. Besides, since the SCN ligands exhibit a high electrochemical stability in a wide range of cathodic potentials, we propose that the SCN ligands would only desorb from the Ag surface without substantial structure transformation.⁴² This is supported by the fact that no signature Raman features from other Ag–S compounds, such as Ag₂S and Ag₂SO₄, have been observed on AgNF-R1 and AgNF-R2 (see Figure S12 in the Supporting Information).⁴¹

Next, we compared the CO₂ reduction performance of AgNF-R1 and AgNF-R2 at -0.7 , -0.9 , -1.1 , and -1.3 V_{RHE}. Their FE_{CO} values were plotted in Figure 4c in comparison with that of AgNF. Under the mild reduction potentials of -0.7 and -0.9 V_{RHE}, the three electrodes have similar FE_{CO}. However, FE_{CO} values of AgNF-R1 and AgNF-R2 drop significantly when more negative reduction potentials are applied. As listed in Table S3 in the Supporting Information, the FE_{CO} of AgNF-R1 declines to 86.5% that of AgNF under -1.1 V_{RHE}, and the FE_{CO} of AgNF-R2 drops to 56.7% . When the potential decreases to -1.3 V_{RHE}, their FE_{CO} values further drop to 56.7 and 32.4% , respectively. Figure 4d shows a similar trend in their j_{CO} values. AgNF has the highest j_{CO} of -33.0 mA cm⁻² at -1.3 V_{RHE}; in comparison, the highest j_{CO} values of AgNF-R1 and AgNF-R2 are only -21.3 and -16.6 mA cm⁻², respectively. ECSAs of the three types of electrodes were measured to evaluate the potential influence of their different porous structures. As shown in Figure S13, the ECSAs of AgNF-R1 and AgNF-R2 drop by 2.8 and 14.3% compared with that of AgNF. The relatively small morphology changes are unlikely the main reason for the observed drastic drop in FE_{CO} and j_{CO} under the potentials of -1.1 and -1.3 V_{RHE}. Table S4 also shows that the changing trend of normalized $j_{\text{CO-ECSA}}$ of the three types of AgNF electrodes under different potentials is similar to that of j_{CO} . Based on the above experimental results, we conclude that anchoring SCN ligands on the Ag surface is

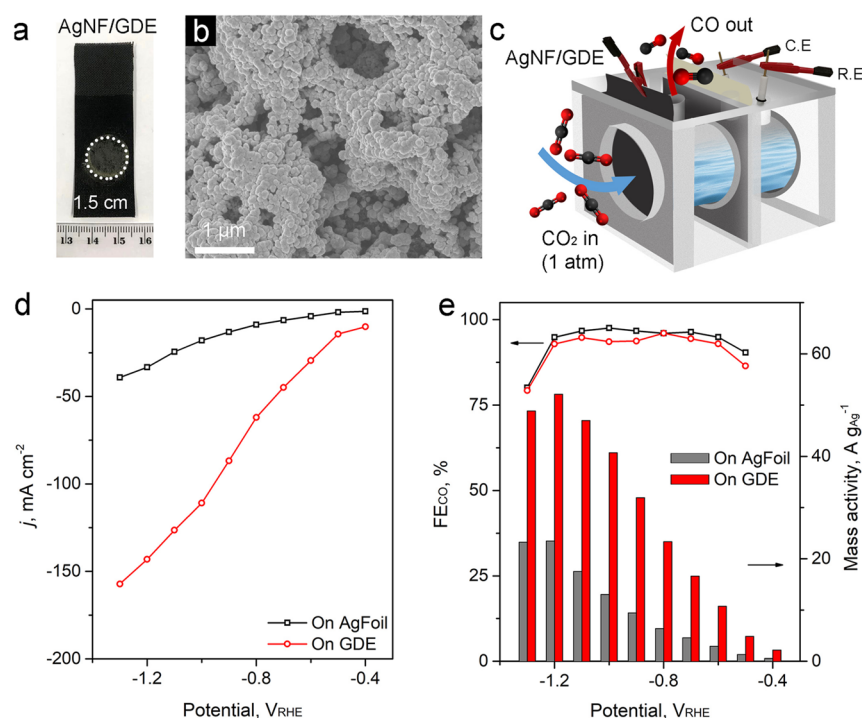


Figure 6. (a) Photo and (b) SEM image of the AgNF/GDE. (c) Schematic illustration of the CO₂RR electrolyzer used in this study. (d) The steady-state current density, (e) selectivity, and mass activity toward CO of the AgNF/GDE electrolyzer obtained at different potentials.

the main reason for the observed CO₂ reduction catalytic activity enhancement of AgNF.

DFT calculations were carried out to gain mechanistic insights into the catalytic activity of AgNF for CO₂RR. According to the famous Sabatier principle, reactant binding energies to metal catalyst surfaces are often correlated with their catalytic activity.^{43–45} The rate-determining step of CO₂ reduction to CO is the formation of COOH* intermediates. Therefore, the adsorption free energy of COOH* (ΔG_{COOH}) has been used as a reactivity descriptor to evaluate the activities of CO₂RR catalysts.^{22,26,46} A Ag₁₄₇ cluster model was adopted in this study since it has shown sufficient to evaluate those much larger NPs by providing suitable undercoordinated sites for CO₂RR.^{26,27} As shown in Figure 5a, Ag particles anchored with SCN ligands were set up to represent the surfaces of AgNF and AgNF-R1 by replacing Ag atoms on corner sites of the Ag₁₄₇ cluster with 12 (denoted as Ag₁₃₅(SCN)₁₂) or 4 SCN ligands (denoted as Ag₁₄₃(SCN)₄). We also assessed if it would be possible to form Ag(SCN)₂ complex by linking two SCN ligands at a single Ag site. However, our calculation results obtained after relaxation suggest such a structure is unstable. Besides, it is noteworthy that the surface coverage of SCN in the cluster models (0.15 for Ag₁₃₅(SCN)₁₂ and 0.0455 for Ag₁₄₃(SCN)₄) is comparable to the experimentally determined values of 0.1884 for AgNF and 0.0358 for AgNF-R1, which shows a good agreement between theoretical models and realistic surfaces. A Ag₁₃₅ cluster without SCN ligands was used to represent the AgNF-R2 sample. Considering the much weaker adsorption of the SCN on the Ag(111) surface than the undercoordinated Ag sites in the Ag clusters, it can be expected that the SCN would exhibit negligible influence on its CO₂RR performance.⁴⁶ Therefore, a clean Ag(111) surface was adopted as a reference in DFT calculations.

Figure 5b shows that SCN ligands cause charge redistribution on Ag surfaces. Compared with Ag₁₄₃(SCN)₄,

Ag₁₃₅(SCN)₁₂ is expected to have a higher density of localized unpaired electrons, which is beneficial for stabilizing surface-adsorbed CO₂⁻ radicals and promoting their subsequent transformation to COOH* after accepting a proton.²⁶ This calculation result correlates with the higher catalytic activity of AgNF observed in our experimental results. The calculated free energy diagram for CO₂ reduction toward CO on these Ag models is shown in Figure 5c. The binding energy of COOH* (ΔG_{COOH}) on Ag₁₃₅(SCN)₁₂ is lower than those on Ag₁₄₇ and Ag(111), indicating improved COOH* adsorption on Ag₁₃₅(SCN)₁₂. It should be noted that the binding energy of CO* (ΔG_{CO}) is similar on the Ag surfaces because CO adsorption follows a donor–acceptor mechanism instead of the radical adsorption mechanism.³⁰

We further investigated HER on these Ag surfaces to understand the improved selectivity toward CO on AgNF. The thermodynamic limiting potentials of CO₂RR and HER ($\Delta U_L = U_{L(\text{CO}_2)} - U_{L(\text{H}_2)}$) on different surfaces were compared to explain their reaction selectivity where U_L is the lowest potential required for all reaction steps to go downhill in the free energy diagram of CO₂RR and HER.^{47,48} Our DFT results (Figure S14 in Supporting Information) suggest that although Ag₁₃₅(SCN)₁₂ has stronger H* binding energy, it exhibits the lowest ΔU_L (Figure 5d), which correlates with the experimentally observed high CO selectivity of AgNF. It is also noteworthy that the density of SCN ligands is critical. The values of ΔU_L gradually decrease on Ag₁₄₃(SCN)₄ and Ag₁₃₅ clusters, suggesting reduced selectivity in CO₂RR. Overall, our DFT calculation results agree with the experiments where the selectivity to CO in CO₂RR on these Ag catalysts follows the order of AgNF > AgNF-R1 > AgNF-R2 > AgNP > Ag foil.

Other than depositing the AgNF on Ag foils, we have also grown AgNF on a carbon-based gas diffusion film electrode with a size of ~1.77 cm² (denoted as AgNF/GDE) by the same synthesis method used for growing AgNF on Ag foils.

Figure 6a shows a photo of AgNF/GDE. AgNF/GDE with larger sizes can be prepared using a high-current power source. The Ag mass loading on the AgNF/GDE is slightly increased to 2.55 mg cm^{-2} compared to AgNF on Ag foils because the carbon film has a rough surface. An SEM image in Figure 6b displays Ag alignments similar to those on Ag foils. Besides, XPS survey scans also show identical surface S and N abundances (i.e., 2.49 and 2.08 at %, respectively) in AgNF on the two types of substrates. These results indicate that the synthesis method of AgNF presented in this study is applicable to different catalyst substrates.

As illustrated in Figure 6c, the CO₂RR performance of AgNF/GDE was assessed in a two-chamber electrolyzer separated with a Nafion 117 membrane. The AgNF/GDE side is open to a CO₂ atmosphere with a partial pressure of 1 atm. The steady-state current densities obtained at different potentials are displayed in Figure 6d. The gas diffusion film helps to overcome the issue related to gaseous CO₂ dissolution and diffusion in aqueous electrolytes, leading to a 4.1–7.5 time increment in the current density in a potential window from -0.4 to $-1.3 \text{ V}_{\text{RHE}}$. Moreover, Figure 6e shows that the excellent selectivity toward CO can be retained. AgNF/GDE can deliver a maximum mass activity of $52.1 \text{ A g}_{\text{Ag}}^{-1}$ at $-1.2 \text{ V}_{\text{RHE}}$, demonstrating an excellent potential for efficient CO production from CO₂RR.

CONCLUSIONS

In summary, we have demonstrated a fast ($\sim 20 \text{ s}$) and efficient electrodeposition method to synthesize hierarchically porous Ag nanofoams with curved surfaces modified by a SCN ligand. The used electrolyte is an aqueous mixture of Ag₂SO₄, KSCN, and (NH₄)₂SO₄. SCN ligands anchored on Ag surfaces demonstrate excellent electrochemical stability under negative potentials. Serving as an electrocatalyst for CO₂RR, AgNF can maintain a high CO selectivity ($\text{FE}_{\text{CO}} > 90\%$) in a wide operation window from -0.5 to $-1.2 \text{ V}_{\text{RHE}}$ and delivers a maximum j_{CO} of 33.0 mA cm^{-2} or a mass activity of $23.5 \text{ A g}_{\text{Ag}}^{-1}$, which is one of the best catalytic performance among recently reported Ag-based electrocatalysts for CO₂RR. Experimental results indicate that SCN ligands are crucial in realizing the high CO selectivity in the wide operation potential window. DFT calculations suggest that the roles of SCN ligands are to promote the formation of COOH* intermediates by inducing charge redistribution on the Ag surfaces. Moreover, the synthesis method of AgNF can be extended to other catalyst substrates. AgNF grown on carbon-based gas diffusion films can overcome the issue related to CO₂ dissolution and diffusion in liquid electrolytes, delivering ~ 2.5 times higher mass activity. This efficient and straightforward Ag catalyst has excellent potentials to be applied in practical CO₂ reduction devices.

ASSOCIATED CONTENT

Supporting Information

The Supporting Information is available free of charge at <https://pubs.acs.org/doi/10.1021/acscatal.9b04633>.

SEM and TEM images of AgNPs; estimation of SCN coverage on AgNFs; XPS spectra of AgSCN and Cl 2p region; typical $j-t$ curves and FE_{CO} values of AgNF, AgNP, and Ag foil obtained at -1.2 V vs RHE; FE_{CO} and FE_{H_2} of Ag catalysts; ECSA measurements; properties and CO₂ electrochemical reduction perform-

ance at -0.6 V vs RHE of various electrodes; performance comparison of various Ag electrocatalysts for CO₂ reduction in aqueous electrolytes; SEM images of the AgNF after 2 h discharging at various potentials; high-resolution XPS spectra of Ag 3d in various samples; HAADF-STEM images, the corresponding EDX elemental maps, Raman spectra, ECSA, FE_{CO} , and CO specific current densities of AgNF-R1 and AgNF-R2; and the free energy diagram of HER on different Ag models (PDF)

AUTHOR INFORMATION

Corresponding Authors

Li Wei – The University of Sydney, Sydney, Australia;
orcid.org/0000-0001-8771-2921; Email: l.wei@sydney.edu.au

Yuan Chen – The University of Sydney, Sydney, Australia;
Email: yuan.chen@sydney.edu.au

Other Authors

Hao Li – The University of Texas at Austin, Austin, Texas
Junsheng Chen – The University of Sydney, Sydney, Australia

Ziwen Yuan – The University of Sydney, Sydney, Australia
Qianwei Huang – The University of Sydney, Sydney, Australia

Xiaozhou Liao – The University of Sydney, Sydney, Australia

Graeme Henkelman – The University of Texas at Austin, Austin, Texas; orcid.org/0000-0002-0336-7153

Complete contact information is available at:

<https://pubs.acs.org/10.1021/acscatal.9b04633>

Notes

The authors declare no competing financial interest.

ACKNOWLEDGMENTS

This study is supported by the Australian Research Council under the Future Fellowships Scheme (FT160100107) and Discovery Programme (DP180102210). L.W. acknowledges support from the Faculty of Engineering and Information Technology of The University of Sydney under the Early Career Researcher Scheme. H.L. and G.H. acknowledge the Welch Foundation (F-1841) and the Texas Advanced Computing Center for supporting computation resources.

REFERENCES

- (1) Centi, G.; Perathoner, S. Opportunities and Prospects in the Chemical Recycling of Carbon Dioxide to Fuels. *Catal. Today* **2009**, *148*, 191–205.
- (2) Arakawa, H.; Aresta, M.; Armor, J. N.; Barteau, M. A.; Beckman, E. J.; Bell, A. T.; Bercaw, J. E.; Creutz, C.; Dinjus, E.; Dixon, D. A.; Domen, K.; DuBois, D. L.; Eckert, J.; Fujita, E.; Gibson, D. H.; Goddard, W. A.; Goodman, D. W.; Keller, J.; Kubas, G. J.; Kung, H. H.; Lyons, J. E.; Manzer, L. E.; Marks, T. J.; Morokuma, K.; Nicholas, K. M.; Periana, R.; Que, L.; Rostrup-Nielsen, J.; Sachtler, W. M. H.; Schmidt, L. D.; Sen, A.; Somorjai, G. A.; Stair, P. C.; Stults, B. R.; Tumas, W. Catalysis Research of Relevance to Carbon Management: Progress, Challenges, and Opportunities. *Chem. Rev.* **2001**, *101*, 953–996.
- (3) Jacobson, M. Z.; Delucchi, M. A. Providing All Global Energy with Wind, Water, and Solar Power, Part I: Technologies, Energy

- Resources, Quantities and Areas of Infrastructure, and Materials. *Energy Policy* **2011**, *39*, 1154–1169.
- (4) Hori, Y. Electrochemical CO₂ Reduction on Metal Electrodes. In *Modern Aspects of Electrochemistry*; Springer: New York, 2008; Vol. 42.
- (5) Sakakura, T.; Choi, J.-C.; Yasuda, H. Transformation of Carbon Dioxide. *Chem. Rev.* **2007**, *107*, 2365–2387.
- (6) Mikkelsen, M.; Jorgensen, M.; Krebs, F. C. The Teraton Challenge. A Review of Fixation and Transformation of Carbon Dioxide. *Energy Environ. Sci.* **2010**, *3*, 43–81.
- (7) Wang, W.; Wang, S.; Ma, X.; Gong, J. Recent Advances in Catalytic Hydrogenation of Carbon Dioxide. *Chem. Soc. Rev.* **2011**, *40*, 3703–3727.
- (8) Qiao, J.; Liu, Y.; Hong, F.; Zhang, J. A Review of Catalysts for the Electrorreduction of Carbon Dioxide to Produce Low-Carbon Fuels. *Chem. Soc. Rev.* **2014**, *43*, 631–675.
- (9) Benson, E. E.; Kubiak, C. P.; Sathrum, A. J.; Smieja, J. M. Electrocatalytic and Homogeneous Approaches to Conversion of CO₂ to Liquid Fuels. *Chem. Soc. Rev.* **2009**, *38*, 89–99.
- (10) Zhang, W.; Hu, Y.; Ma, L.; Zhu, G.; Wang, Y.; Xue, X.; Chen, R.; Yang, S.; Jin, Z. Progress and Perspective of Electrocatalytic CO₂ Reduction for Renewable Carbonaceous Fuels and Chemicals. *Adv. Sci.* **2018**, *5*, 1700275.
- (11) Schulz, H. Short History and Present Trends of Fischer-Tropsch Synthesis. *Appl. Catal., A* **1999**, *186*, 3–12.
- (12) Dry, M. E. The Fischer-Tropsch Process: 1950-2000. *Catal. Today* **2002**, *71*, 227–241.
- (13) Rakowski DuBois, M.; DuBois, D. L. Development of Molecular Electrocatalysts for CO₂ Reduction and H₂ Production/Oxidation. *Acc. Chem. Res.* **2009**, *42*, 1974–1982.
- (14) Kostecki, R.; Augustynski, J. Electrochemical Reduction of CO₂ at An Activated Silver Electrode. *Ber. Bunsen-Ges. Phys. Chem.* **1994**, *98*, 1510–1515.
- (15) Hatsukade, T.; Kuhl, K. P.; Cave, E. R.; Abram, D. N.; Jaramillo, T. F. Insights into the Electrocatalytic Reduction of CO₂ on Metallic Silver Surfaces. *Phys. Chem. Chem. Phys.* **2014**, *16*, 13814–13819.
- (16) Lu, Q.; Rosen, J.; Zhou, Y.; Hutchings, G. S.; Kimmel, Y. C.; Chen, J. G.; Jiao, F. A Selective and Efficient Electrocatalyst for Carbon Dioxide Reduction. *Nat. Commun.* **2014**, *5*, 3242.
- (17) Hsieh, Y.-C.; Senanayake, S. D.; Zhang, Y.; Xu, W.; Polyansky, D. E. Effect of Chloride Anions on the Synthesis and Enhanced Catalytic Activity of Silver Nanocoral Electrodes for CO₂ Electroreduction. *ACS Catal.* **2015**, *5*, 5349–5356.
- (18) Hoshi, N.; Kato, M.; Hori, Y. Electrochemical Reduction of CO₂ on Single Crystal Electrodes of Silver Ag(111), Ag(100) and Ag(110). *J. Electroanal. Chem.* **1997**, *440*, 283–286.
- (19) Salehi-Khojin, A.; Jhong, H.-R. M.; Rosen, B. A.; Zhu, W.; Ma, S.; Kenis, P. J. A.; Masel, R. I. Nanoparticle Silver Catalysts That Show Enhanced Activity for Carbon Dioxide Electrolysis. *J. Phys. Chem. C* **2013**, *117*, 1627–1632.
- (20) Dutta, A.; Morstein, C. E.; Rahaman, M.; Cedeño López, A.; Broekmann, P. Beyond Copper in CO₂ Electrolysis: Effective Hydrocarbon Production on Silver-Nanofoam Catalysts. *ACS Catal.* **2018**, *8*, 8357–8368.
- (21) Gao, J.; Zhu, C.; Zhu, M.; Fu, Y.; Huang, H.; Liu, Y.; Kang, Z. Highly Selective and Efficient Electroreduction of Carbon Dioxide to Carbon Monoxide with Phosphate Silver-Derived Coral-like Silver. *ACS Sustainable Chem. Eng.* **2019**, *7*, 3536–3543.
- (22) Liu, S.; Tao, H.; Zeng, L.; Liu, Q.; Xu, Z.; Liu, Q.; Luo, J.-L. Shape-Dependent Electrocatalytic Reduction of CO₂ to CO on Triangular Silver Nanoplates. *J. Am. Chem. Soc.* **2017**, *139*, 2160–2163.
- (23) Rosen, J.; Hutchings, G. S.; Lu, Q.; Rivera, S.; Zhou, Y.; Vlachos, D. G.; Jiao, F. Mechanistic Insights into the Electrochemical Reduction of CO₂ to CO on Nanostructured Ag Surfaces. *ACS Catal.* **2015**, *5*, 4293–4299.
- (24) Zhang, L.; Wang, Z.; Mehio, N.; Jin, X.; Dai, S. Thickness- and Particle-Size-Dependent Electrochemical Reduction of Carbon Dioxide on Thin-Layer Porous Silver Electrodes. *ChemSusChem* **2016**, *9*, 428–432.
- (25) Hu, L.; Zhang, Y.; Han, W. Boosting CO₂ Electroreduction Over Silver Nanowires Modified by Wet-Chemical Sulfidation and Subsequent Electrochemical De-sulfidation. *New J. Chem.* **2019**, *43*, 3269–3272.
- (26) Kim, C.; Jeon, H. S.; Eom, T.; Jee, M. S.; Kim, H.; Friend, C. M.; Min, B. K.; Hwang, Y. J. Achieving Selective and Efficient Electrocatalytic Activity for CO₂ Reduction Using Immobilized Silver Nanoparticles. *J. Am. Chem. Soc.* **2015**, *137*, 13844–13850.
- (27) Kim, C.; Eom, T.; Jee, M. S.; Jung, H.; Kim, H.; Min, B. K.; Hwang, Y. J. Insight into Electrochemical CO₂ Reduction on Surface-Molecule-Mediated Ag Nanoparticles. *ACS Catal.* **2017**, *7*, 779–785.
- (28) Lim, H.-K.; Shin, H.; Goddard, W. A., III; Hwang, Y. J.; Min, B. K.; Kim, H. Embedding Covalency into Metal Catalysts for Efficient Electrochemical Conversion of CO₂. *J. Am. Chem. Soc.* **2014**, *136*, 11355–11361.
- (29) Weaver, M. J.; Barz, F.; Gordon, J. G., II; Philpott, M. R. Surface-enhanced Raman Spectroscopy of Electrochemically Characterized Interfaces: Potential Dependence of Raman Spectra for Thiocyanate at Silver Electrodes. *Surf. Sci.* **1983**, *125*, 409–428.
- (30) Gold, H. S.; Buck, R. P. A Raman Spectroscopic Study of Complexes of Thiocyanate at the Silver Electrode Surface. *J. Raman Spectrosc.* **1979**, *8*, 323–325.
- (31) Hupp, J. T.; Larkin, D.; Weaver, M. J. Specific Adsorption of Halide and Pseudohalide Ions at Electrochemically Roughened versus Smooth Silver-Aqueous Interfaces. *Surf. Sci.* **1983**, *125*, 429–451.
- (32) Cherevko, S.; Chung, C.-H. Impact of Key Deposition Parameters on the Morphology of Silver Foams Prepared by Dynamic Hydrogen Template Deposition. *Electrochim. Acta* **2010**, *55*, 6383–6390.
- (33) Cherevko, S.; Xing, X.; Chung, C.-H. Electrodeposition of Three-Dimensional Porous Silver Foams. *Electrochem. Commun.* **2010**, *12*, 467–470.
- (34) Perdew, J. P.; Burke, K.; Ernzerhof, M. Generalized Gradient Approximation Made Simple. *Phys. Rev. Lett.* **1996**, *77*, 3865–3868.
- (35) Kohn, W.; Sham, L. J. Self-Consistent Equations Including Exchange and Correlation Effects. *Phys. Rev.* **1965**, *140*, A1133–A1138.
- (36) Monkhorst, H. J.; Pack, J. D. Special Points for Brillouin-Zone Integrations. *Phys. Rev. B* **1976**, *13*, 5188–5192.
- (37) Gao, D.; Zhou, H.; Wang, J.; Miao, S.; Yang, F.; Wang, G.; Wang, J.; Bao, X. Size-Dependent Electrocatalytic Reduction of CO₂ over Pd Nanoparticles. *J. Am. Chem. Soc.* **2015**, *137*, 4288–4291.
- (38) Plowman, B. J.; Jones, L. A.; Bhargava, S. K. Building with Bubbles: the Formation of High Surface Area Honeycomb-Like Films via Hydrogen Bubble Templated Electrodeposition. *Chem. Commun.* **2015**, *51*, 4331–4346.
- (39) Nyquist, R. A.; Kagel, R. O. *Handbook of Infrared and Raman Spectra of Inorganic Compounds and Organic Salts: Infrared Spectra of Inorganic Compounds*; Academic press, 2012; Vol. 4.
- (40) Gonnissen, D.; Langenaeker, W.; Hubin, A.; Geerlings, P. A. (Surface-Enhanced) Raman Spectroscopic Study of the Adsorption of S₂O²⁻ and SCN⁻ on A Silver Deposit. *J. Raman Spectrosc.* **1998**, *29*, 1031–1039.
- (41) Martina, I.; Wiesinger, R.; Jembrih-Simbürger, D.; Schreiner, M. Micro-Raman Characterisation of Silver Corrosion Products: Instrumental Set Up and Reference Database. *e-Preserv. Sci.* **2012**, *9*, 1–8.
- (42) Gorska, B.; Bujewska, P.; Fic, K. Thiocyanates as Attractive Redox-Active Electrolytes for High-Energy and Environmentally-Friendly Electrochemical Capacitors. *Phys. Chem. Chem. Phys.* **2017**, *19*, 7923–7935.
- (43) Li, H.; Henkelman, G. Dehydrogenation Selectivity of Ethanol on Close-Packed Transition Metal Surfaces: A Computational Study of Monometallic, Pd/Au, and Rh/Au Catalysts. *J. Phys. Chem. C* **2017**, *121*, 27504–27510.

(44) Li, H.; Shin, K.; Henkelman, G. Effects of Ensembles, Ligand, and Strain on Adsorbate Binding to Alloy Surfaces. *J. Chem. Phys.* **2018**, *149*, 174705.

(45) Li, H.; Luo, L.; Kunal, P.; Bonifacio, C. S.; Duan, Z.; Yang, J. C.; Humphrey, S. M.; Crooks, R. M.; Henkelman, G. Oxygen Reduction Reaction on Classically Immiscible Bimetallics: A Case Study of RhAu. *J. Phys. Chem. C* **2018**, *122*, 2712–2716.

(46) Back, S.; Yeom, M. S.; Jung, Y. Active Sites of Au and Ag Nanoparticle Catalysts for CO₂ Electroreduction to CO. *ACS Catal.* **2015**, *5*, 5089–5096.

(47) Kim, D.; Xie, C.; Becknell, N.; Yu, Y.; Karamad, M.; Chan, K.; Crumlin, E. J.; Nørskov, J. K.; Yang, P. Electrochemical Activation of CO₂ through Atomic Ordering Transformations of AuCu Nanoparticles. *J. Am. Chem. Soc.* **2017**, *139*, 8329–8336.

(48) Ren, W.; Tan, X.; Yang, W.; Jia, C.; Xu, S.; Wang, K.; Smith, S. C.; Zhao, C. Isolated Diatomic Ni-Fe Metal-Nitrogen Sites for Synergistic Electroreduction of CO₂. *Angew. Chem., Int. Ed.* **2019**, *58*, 6972–6976.